Physics of the Earth and Planetary Interiors 308 (2020) 106582

Contents lists available at ScienceDirect

Physics of the Earth and Planetary Interiors

journal homepage: www.elsevier.com/locate/pepi

One-off deep crustal earthquake swarm in a stable intracontinental region of the southwestern Korean Peninsula

Tae-Kyung Hong[a,*], Seongjun Park[a], Junhyung Lee[a], Dongchan Chung[a], Woohan Kim[b]

[a] Department of Earth System Sciences, Yonsei University, 50 Yonsei-ro, Seodaemun-gu Seoul, 03722, South Korea
[b] Department of Earth and Environmental Sciences and RINS, Gyeongsang National University, Gyeongsangnam-do 52828, South Korea

ARTICLE INFO

Keywords:
Deep crustal
Earthquake swarm
Korean peninsula
Intracontinental
Transiently active

ABSTRACT

A deep crustal strike-slip earthquake swarm that occurred in the intracontinental region of the southwestern Korean Peninsula is investigated. The earthquakes are detected using matched filter analysis. The hypocenters are then refined, showing more than 500 micro to small strike-slip earthquakes concentrated on a fault plane with dimensions of 500 m by 300 m at a depth of ~21 km. The low temperature in the source depth facilitates the seismicity. The earthquake swarm was transiently active for 15 days from 25 April 2020 to 12 May 2020, presenting a high seismicity rate with a Gutenberg-Richter b value of 2.01 (± 0.05). The earthquake swarm began in the central area and expanded outward with time. The spatiotemporal seismicity distribution reflects bilateral rupture. The focal mechanism solutions suggest a left-lateral strike-slip fault with a strike of 103.6° ± 3.2° and a dip of 73.3° ± 11.7°. The spatial distribution of seismicity generally agrees with the focal mechanism solutions. The orientation of the inverted stress field agrees with the ambient stress field, suggesting that the earthquake swarm occurred as a consequence of ambient lithostatic stress loading. Coulomb stress changes suggest that the stress increased in the directions of WNW-ESE and NNE-SSW from the fault. The transiently active earthquake swarm began to occur after the 2011 M_W9.0 Tohoku-Oki megathrust earthquake, suggesting a rapid release of accumulated stress in response to changes in the properties of the medium caused by the megathrust earthquake.

1. Introduction

The tectonic loading rate in stable continental regions is low, and thus, the earthquake occurrence frequency in intracontinental regions is lower than in interplate regions. Large earthquakes may still occur within geological structures in stable continental regions (Calais et al., 2016). Most earthquakes in the continental lithosphere occur in the upper crust, while mid- to lower crustal earthquakes rarely occur in intraplate regions because ductile deformation is expected (Gardonio et al., 2018). However, earthquakes are not limited to the brittle crust. It was previously reported that weakening in a ductile regime can produce earthquakes (Prieto et al., 2017).

Deep crustal fluids may trigger large lower crustal earthquakes in an intraplate region (Gardonio et al., 2018). A normal-faulting event with a moment magnitude of M_W6.5 occurred as a result of deep fluids (Gardonio et al., 2018). Additionally, glacial isostatic adjustment most likely triggers deep crustal earthquakes (Brandes et al., 2018). It was suggested that a decollement between the crust and the mantle may play a role in producing faulting in the lower crust (Leyton et al., 2009). A cratonic collision may also cause crustal-scale thrust faults to be reactivated in tension, producing normal-faulting earthquakes (Kolawole et al., 2017).

A previous study proposed the possible presence of a reservoir of elastic stress that can be released episodically by deep fluid migration (Gardonio et al., 2018). Thermal elasticity may contribute to such a stress reservoir (Calais et al., 2016). Major earthquakes may occur when the cumulative stress from tectonic loading reaches the failure threshold. However, various examples have presented the temporal clustering of major earthquakes in a stable intraplate regime (Stein and Mazzotti, 2007; Li et al., 2009).

Recently, it was reported that the transient perturbation of the local stress or fault strength can result in the release of elastic energy from the prestressed lithosphere (Calais et al., 2016). It was also suggested that a small change in the stress field may cause a significant seismicity change (Stein, 1999). Furthermore, thermal elasticity may bring the continental crust close to failure (Calais et al., 2016).

Earthquakes may occur in regions without previous seismicity or surface evidence of strain accumulation. Thus, seismicity may be more

* Corresponding author.
E-mail address: tkhong@yonsei.ac.kr (T.-K. Hong).

https://doi.org/10.1016/j.pepi.2020.106582
Received 9 July 2020; Received in revised form 1 September 2020; Accepted 1 September 2020
Available online 09 September 2020

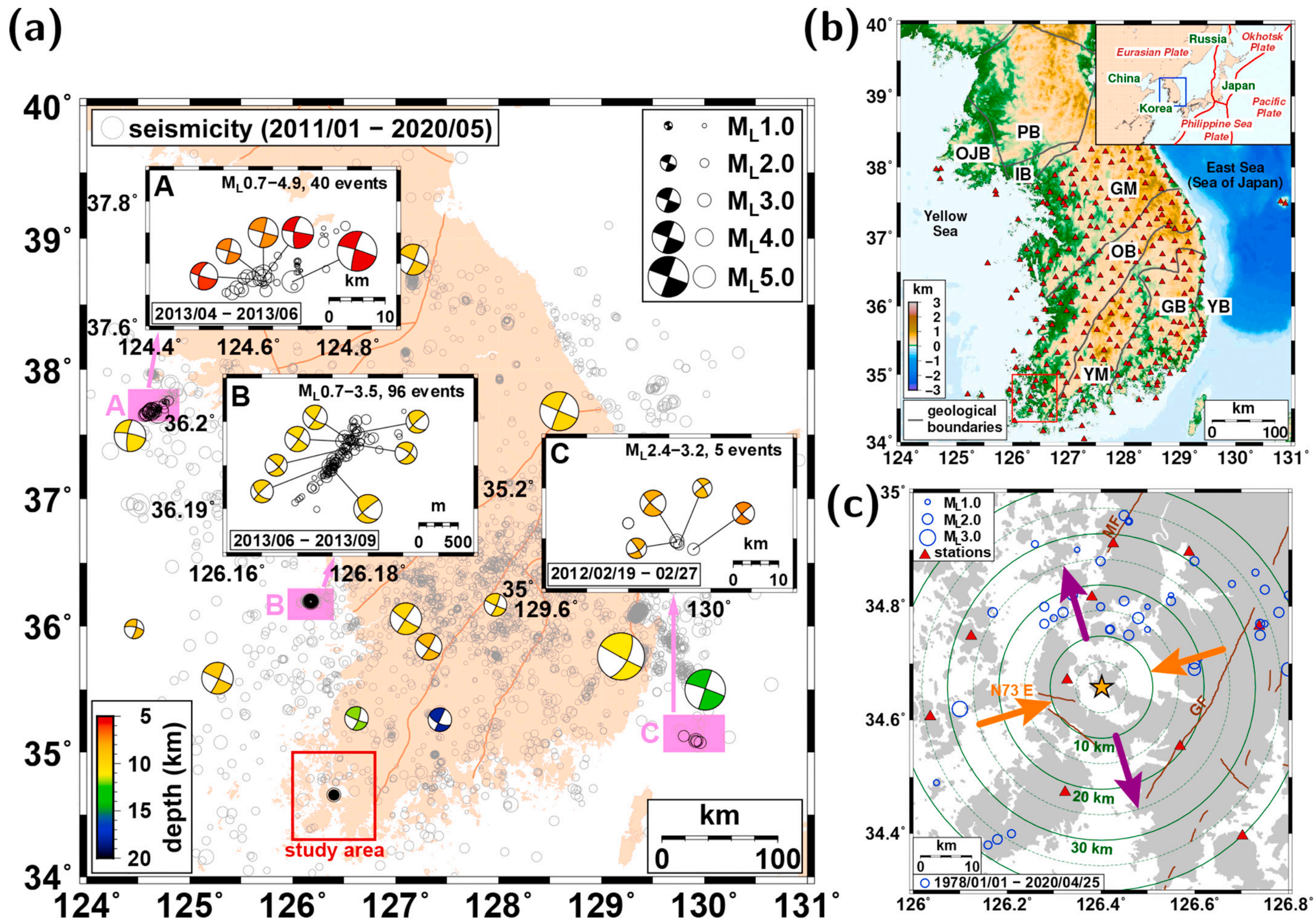

Fig. 1. (a) Map of earthquake swarm regions (A, B, and C) and seismicity. The insets present enlarged views of the earthquake distribution in the earthquake swarm regions. The study region with an earthquake swarm is marked with a rectangular area. (b) Distribution of seismic stations (triangles) and surface topography. The major geological provinces are denoted: Gyeonggi massif (GM), Gyeongsang basin (GB), Imjingang belt (IB), Okcheon belt (OB), Ongjin basin (OJB), Yeongnam massif (YM), and Yeonil basin (YB). (c) Distribution of earthquakes, the ambient stress field, and the major faults in the study region. The location of the earthquake swarm is marked with a star. Major faults include the Gwangju fault (GF) and Muan fault (MF). The ambient stress field is composed of N73°*E*-directed compression and N17°W-directed tension.

spatially distributed than suggested by geodetic strain rates and paleoearthquake distribution. Earthquakes in stable continental regions release strain from the prestressed lithosphere, where faults are in a state of failure equilibrium. Such earthquakes may be triggered by small transient stress changes caused by surface load variations or the diffusion of fluids in the crust (Calais et al., 2016).

The required stress for brittle faulting is dependent on the lithology and rheology of the medium. Thermal-elastic stresses in excess of 100 MPa can be stored in the crust during the burial of granite, emplacing the buried rock in a highly prestressed state (Schrank et al., 2012). Approximately 10% of the total elastic energy is dissipated below 400°C with relaxation times reaching millions of years (Calais et al., 2016).

Brittle failure is mainly controlled by temperature (McKenzie et al., 2005). The occurrence of earthquakes generally means that the typical earthquake spawning environment characteristics, such as the temperature, is satisfied. Deep-crustal earthquakes are controlled by lithospheric temperatures (Wong and Chapman, 1990). The upper temperature bound for brittle faulting in the crust is approximately 250–450°C (Chen and Molnar, 1983). The maximum allowable temperatures for earthquakes to occur in the crust and upper mantle are 350 ± 100°C and 700 ± 100°C, respectively (Brace and Byerlee, 1970; Chen and Molnar, 1983; Wong and Chapman, 1990).

The temperature constrains the focal depth (cutout depth) (Brace and Byerlee, 1966; Bonner et al., 2003). The cutout depth in California was reported to be 450 ± 50°C and 260 ± 40°C depending on the location (Bonner et al., 2003). The brittle-ductile transition zone is referred to as 300 ± 50°C (Bonner et al., 2003). The brittle-ductile transition in oceanic lithosphere appears at approximately 600°C (McKenzie et al., 2005). Heat flow may control the temperature. For example, heat flows of 9–15 mWm^{-2} at the Moho may produce an environment with a seismic cutoff temperature of 350°C at a depth of 28 ± 4 km (Veikkolainen et al., 2017).

The occurrence of deep crustal earthquake swarms in stable intracontinental regions remains a topic of interest. Here, we investigate the fault properties and seismogenic mechanism of an earthquake swarm in the southwestern Korean Peninsula.

2. Geology and earthquake swarms

The Korean Peninsula and its neighboring regions belong to a stable intracontinental regime located in the eastern Eurasian plate. The Korean Peninsula was formed by a continental collision between the North China and South China blocks during the late Permian to Jurassic, which was followed by continental rifting and the opening of the East Sea (Sea of Japan) during the Oligocene to mid-Miocene (Jolivet et al., 1994; Chough et al., 2000; Oh, 2006). This continental collision developed NE-trending geological provinces.

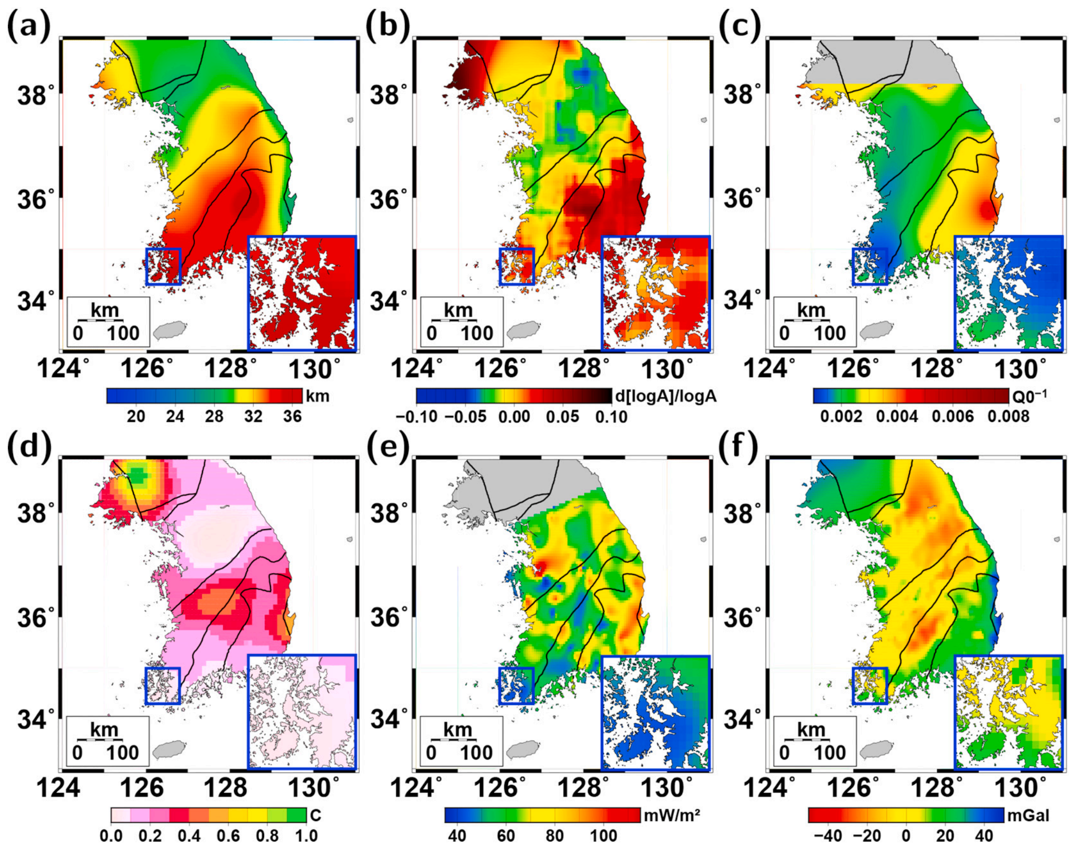

Fig. 2. Regional variations in the seismic and geophysical models: (a) crustal thickness (Hong et al., 2008), (b) crustal *P* amplification (Hong and Lee, 2012), (c) crustally guided shear-wave attenuation ($Lg\ Q_0^{-1}$) (Hong, 2010), (d) seismic densities of earthquakes with magnitudes equal to or larger than 2.5 in 1978–2019 (Park et al., 2020), (e) surface heat flows (Lee et al., 2010), and (f) Bouguer gravity anomalies (Cho et al., 1997). The earthquake swarm region is marked with the rectangle. Insets show the enlarged models.

The Korean Peninsula and Yellow Sea are characterized by continental crust with a thickness of 29–36 km (Hong et al., 2008; Hong and Kang, 2009; Jo and Hong, 2013). On the other hand, the East Sea (Sea of Japan) has a transitional crustal structure between continental crust and oceanic crust. The crustal thickness in the East Sea is 8.5–14 km (Hirata et al., 1992; Kim et al., 1998; Furumura et al., 2014; Hong et al., 2020). The rate of seismicity is low, and the seismicity is spatially diffuse. The focal depths of these events are 4–20 km, mostly within ~4–8 km in the peninsula and Yellow Sea and 2–30 km (mostly 12–20 km) in the East Sea (Hong et al., 2016, 2020). The ambient stress field is composed of ENE-directed compression and SSE-directed tension (Choi et al., 2012; Lee et al., 2017).

The 2011 M_W9.0 Tohoku-Oki megathrust earthquake occurred in the Japan Trench, which is ~1200 km from the Korean Peninsula. This earthquake produced coseismic lithospheric displacements of ~4 cm along the eastern coast and ~2 cm along the western coast of the Korean Peninsula (Kim and Bae, 2012; Zhao et al., 2012; Hong et al., 2015). Postseismic displacements followed these coseismic displacements for > 3 years (Kim et al., 2016a; Hong et al., 2017a). The resulting distinctive crustal extension produced a transient extensional stress field over the Korean Peninsula (Hong et al., 2015). The crustal seismic velocity in the Korean Peninsula decreased abruptly after the 2011 megathrust earthquake but recovered gradually with time (Hong et al., 2017a).

Earthquakes occurred episodically during the transmission of strong seismic waves from the 2011 megathrust earthquake (Houng et al., 2016). Additionally, the seismicity appeared to increase after the megathrust earthquake (Hong et al., 2015, 2018), following which earthquakes occurred in both high-seismicity and low-seismicity regions. In the Yellow Sea (Fig. 1), episodic earthquake swarms occurred in two regions (regions A and B) (Hong et al., 2015). Another earthquake swarm occurred in a region off the southeastern peninsula in 2012 (region C). The earthquake swarm in region A lasted for 60 days beginning on 29 April 2013. Forty-five earthquakes with magnitudes of M_L0.7–4.9 were identified (Hong et al., 2015). The earthquake swarm in region B was composed of 108 earthquakes with magnitudes of M_L0.7–3.5 spanning 120 days beginning on 2 June 2013.

The abovementioned increase in seismicity may be associated with a transient decrease in the yield strength due to distinct crustal extension (Hong et al., 2015). Changes in the properties of the medium caused major earthquakes to occur at relatively early times. Successive M_L5 earthquakes occurred on the outskirts of high-seismicity regions (Hong et al., 2018). Observations of earthquakes in low-seismicity regions suggest that changes in the transient properties of the medium facilitate the occurrence of earthquakes at low failure thresholds (Watts and Burov, 2003; Hong et al., 2015, 2018).

An earthquake swarm has affected the southwestern Korean Peninsula since late April 2020. The earthquakes were clustered in a small region (Fig. 1). The largest event was the M_L3.1 earthquake that struck on 3 May 2020. Notably, the earthquake source region has been seismically quiescent since 1978, when the national seismic monitoring program began operation. No events have been reported in the region with a radius of 15 km (Fig. 1).

The source region belongs to the Okcheon belt between the Gyeonggi and Yeongnam massifs (Fig. 1) (Chough et al., 2000; Hong et al., 2016). The ambient stress field is composed of N73°*E*-directed compression and N17°W-directed tension. There are two major faults 20 km away from the source region (National Emergency Management Agency, 2012). These faults were most recently reactivated during the Paleogene.

The expected maximum magnitude of the source region is 4.65–5.04 according to a seismotectonic province model (Hong et al., 2016). The expected maximum magnitude is the lowest in the Korean Peninsula. The Gutenberg-Richter *b* value of the seismotectonic province for the source region was 1.25 before the earthquake swarm. It is worth noting that the *b* value for the whole peninsula is 0.92 (Hong et al., 2016).

The earthquake source region presents a large crustal thickness of ~36 km, low *Lg* attenuation, and high *P* amplification but no apparent gravity anomalies (Fig. 2). These observations suggest that the source region has a low temperature, and the thick crust may be composed of high density materials satisfying isostatic equilibrium. The surface heat flow in the source region is 40–50 mW/m^2, which is lower than that in other areas within the Korean Peninsula (Fig. 2). This heat flow suggests that the temperature at a depth of ~21 km is approximately 205°C considering the thermal properties of the Korean Peninsula (Lee et al., 2010). These temperatures are sufficiently low to accommodate seismicity in the deep crust (Bonner et al., 2003).

3. Methods

We refine the hypocentral parameters of earthquakes using a source-parameter inversion method, VELHYPO that jointly inverts the hypocentral parameters and velocity structures (Kim et al., 2014, 2016b). This method is particularly effective for regions with poorly known velocity structures (Kim et al., 2016b). We use the initial source parameters of the earthquakes reported by the KMA. We jointly determine the hypocentral location and velocity structure for each event.

We then apply a matched filter analysis to search for additional small to micro earthquakes (Gibbons and Ringdal, 2006; Shelly et al., 2007; Peng and Zhao, 2009). The seismic waveforms are bandpass-filtered between 2 and 16 Hz. We analyze the seismic records from 7 stations at distances of less than 50 km from the 28 April 2020 M_L2.1 earthquake epicenter to detect additional events.

We align the seismic waveforms as a function of both time and distance for the location of a reference earthquake. We apply cross-correlation between the template waveforms and continuous waveforms. We select the template waveforms from a reference earthquake for each station. Considering the waveform duration, we use 2-s-long template waveforms that begin 0.1 s before the phase arrival times.

We stack the correlation functions over the stations for each component when the seismic signals are identifiable. The *S* phase is identified for all components of all stations. The *P* phase is weaker than the *S* phase. Hence, we analyze only the vertical component record for the *P* phase. We search the seismic signals with correlation coefficients greater than 9 times the median correlation coefficient for background noise. When we find seismic signals satisfying the given criteria, we declare that an event is detected.

After an event is detected, we search for *P* and *S* waves at 36 stations at distances less than ~112 km. We refine the arrival times of the *P* and *S* waves at each station using the phase correlation with the template waveforms. We search for *S* waves in the range from −0.2 to 0.2 s for the reference traveltime, and we search for *P* waves in the range from −0.1 to 0.1 s.

The traveltime differences with respect to the template waveforms are applied to a double-difference method (hypoDD) for the determination of event locations (Waldhauser and Ellsworth, 2000). We use the refined location of the reference earthquake for the initial event locations. Here, we consider possible variations of ± 1 km for the reference focal depth considering the depth error depending on the velocity model. We implement a 1-D velocity model for the hypocenter inversion (Kennett et al., 1995).

We determine the event magnitude using an amplitude scaling factor of the matched waveforms of the detected events with respect to the template waveforms of the reference earthquake (Gibbons and Ringdal, 2006). The relationship between the local magnitude scale and amplitude scaling factor is given by

$$M_L = a(\log\gamma)^3 + b(\log\gamma)^2 + c(\log\gamma) + d, \quad (1)$$

where γ is the amplitude scaling factor, and *a*, *b*, *c*, and *d* are constants to be determined by region. The amplitude scaling factor (γ) is determined by averaging the amplitude ratios with weighting factors. We use the correlation coefficients of the waveforms for the weighting factors.

We determine the Gutenberg-Richter frequency-magnitude relationship for earthquakes as follows (Aki, 1965):

$$\log N = a - bM, \quad (2)$$

where *a* and *b* are constants, *M* is the magnitude, and *N* is the number of events with magnitudes greater than or equal to *M*. We determine the constants *a* and *b* using the maximum likelihood method (Bender, 1983; Wiemer and Wyss, 2000). We determine the focal mechanism solutions of small-size earthquakes using phase polarity analysis (Snoke, 2002).

We determine the Coulomb stress changes induced by the earthquake swarm. The Coulomb stress changes present the level of shear stress changes on the faults in the considered orientation and motion sense. The Coulomb stress change ΔCFS induced by an earthquake is given by (Toda et al., 2005)

$$\Delta\mathrm{CFS} = \Delta\tau - \mu'\Delta\sigma_n, \quad (3)$$

where $\Delta\tau$ is the shear stress change, μ' is the effective frictional coefficient, and $\Delta\sigma_n$ is the normal stress change (positive for increased compression). The effective frictional coefficient μ' is set to 0.4 (Nalbant et al., 1998; Hong et al., 2015, 2017b). The ambient compressional stress field is oriented N73°E, and the strength is 6.5 MPa (Hong et al., 2015, 2017b; Lee et al., 2017). The lithospheric Young's modulus is set to 80 GPa, and Poisson's ratio is 0.25 (King et al., 1994; Hong et al., 2015).

4. Data

The national seismic monitoring in the Korean Peninsula began in 1978. The number of seismic stations increased continuously with time. The seismic stations are deployed densely over the peninsula (Fig. 1). The Korea Meteorological Administration reported 75 events of the earthquake swarm in April to May 2020.

We collect the source information of the earthquakes from the Korea Meteorological Administration. The reported magnitudes of the events are M_L0.9–3.1. We choose velocity (broadband and short-period) and acceleration records from seismic stations in a region with a radius of 200 km from the earthquakes (Fig. 1). We collect continuous seismic records from the Korea Meteorological Administration (KMA) and the Korea Institute of Geoscience and Mineral Resources (KIGAM) from 9 April 2020 to 23 May 2020.

5. Procedure and magnitude scaling

We first refine the event locations and origin times of reported earthquakes using a hypocentral-parameter inversion method (VELHYPO) based on manually picked phase arrival times. We further search earthquakes swarm from continuous records using a matched filter analysis based on the waveforms of a reference event (Fig. 3). Seismic records analyzed in this study are bandpass filtered between 2 and 16 Hz considering the frequency contents of micro events. The event locations and arrival times of all detected events are determined using a double difference method (hypoDD).

We determine the magnitudes of detected events using amplification (amplitude scaling factor) of the matched waveforms of the detected events with respect to the template waveforms of the reference earthquake. We use the 28 April 2020 M_L2.1 earthquake as the reference event. The amplitude scaling factor (γ) is determined by weighed averages of amplitude ratios between the matched waveforms of detected event and the template waveforms of the reference

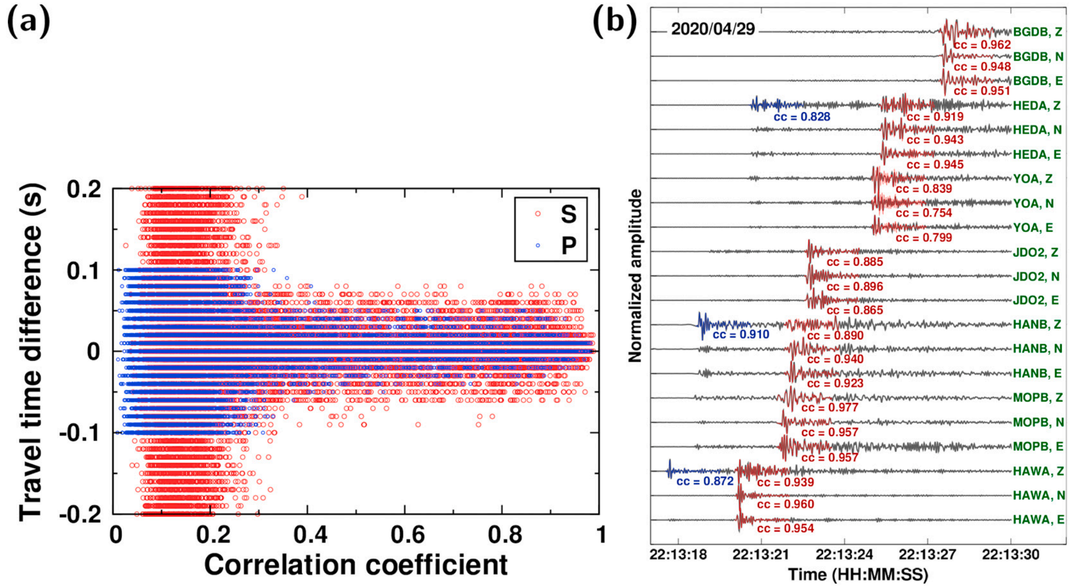

Fig. 3. Event detection using matched filter analysis: (a) correlation coefficients and traveltime differences for matched *P* and *S* signals and (b) example of detected signals. The signals are well detected among all three components.

earthquake. The correlation coefficients of the matched waveforms are used for weighting factors. For the stable determination of magnitudes, we analyze only the *S* waves with correlation coefficients greater than 0.3.

We determine a local magnitude scaling equation based on the phase amplitudes of 75 earthquakes with known magnitudes. The *S* waveforms at 36 stations in distances less than 112 km are analyzed. The local magnitude scaling equation is determined by (Fig. 4)

$$M_L = a(\log\gamma)^3 + b(\log\gamma)^2 + c(\log\gamma) + d, \quad (4)$$

where γ is the amplitude scaling factor and the constants are $a = 0.124$ (± 0.044), $b = 0.568$ (± 0.120), $c = 1.054$ (± 0.097), and $d = 2.085$ (± 0.048).

6. Earthquake detection and source-parameter refinement

Events began to occur on 25 April 2020. The largest event was the M_L3.1 earthquake that occurred on 3 May 2020. We refine the source locations of 15 earthquakes with magnitudes $\geq M_L$1.7 using VELHYPO (Kim et al., 2014, 2016b). The relocated locations are placed in a region spanning ~500 m by 500 m (Fig. 5). The events are generally clustered within a small radius.

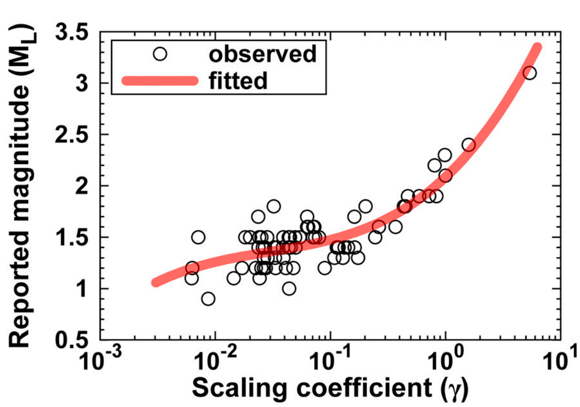

Fig. 4. Relationship between the reported magnitude (M_L) and scaling coefficient (γ). The relationship is reasonably represented by a third-order polynomial.

We choose the 28 April 2020 M_L2.1 event as the reference earthquake to detect events using matched filter analysis. The 28 April 2020 M_L2.1 event occurred near the 3 May 2020 M_L3.1 event. The M_L2.1 event provides better template waveforms for the detection of micro events than the M_L3.1 event due to the inherent magnitude dependence of the frequency contents.

We perform a matched filter analysis to detect micro events from continuous three-component records of 7 stations in distances less 50 km from the earthquake swarm. The matched filter analysis employs slant-stacking of cross correlation functions along the traveltimes of phases. We find 527 events from the matched filter analysis. The events are temporally clustered in an earthquake swarm that was active once over a time period of 17 days. A couple of small events followed the earthquake swarm.

We analyze 18,910 three-component waveforms of 36 stations in distances less than 112 km to determine the phase traveltimes at all available stations. We search the phase arrival times at stations considering the phase traveltimes of the reference event from cross-correlation functions stacked over three components. The *P* and *S* waves at stations are searched in time ranges of −0.1 to 0.1 s and − 0.2 to 0.2 s for the reference *P* and *S* traveltimes, respectively (Fig. 3).

We determine the event locations using the double-difference method (hypoDD). Here, the stacked correlation coefficient at each station is used for a weighting factor in the hypocentral-parameter inversion based on hypoDD. The event locations are clustered (Fig. 6). The epicenters are more concentrated than those determined using VELHYPO (Fig. 5). The double-difference method relocates the events so that they are spatially clustered. Subsequent events are generally placed nearby. The event magnitudes are estimated using the local magnitude scaling equation based on amplitude scaling factor with respect to the reference earthquake. The event magnitudes range between M_L0.1 and 3.1 (Fig. 7).

We determine the Gutenberg-Richter frequency-magnitude relationship for the earthquake swarm using the maximum likelihood method (Bender, 1983; Wiemer and Wyss, 2000). We find that the Gutenberg-Richter *b* value is 2.01 (± 0.05) (Fig. 7). The minimum magnitude to ensure complete event detection is M_L1.1. The *b* value is larger than that of the background seismicity in the Korean Peninsula, ~0.92 (Hong et al., 2016). A large *b* value means frequent occurrence of small events. The observation of unusual earthquake swarm and large *b* value suggests that the stress accumulated in the fault region is emitted

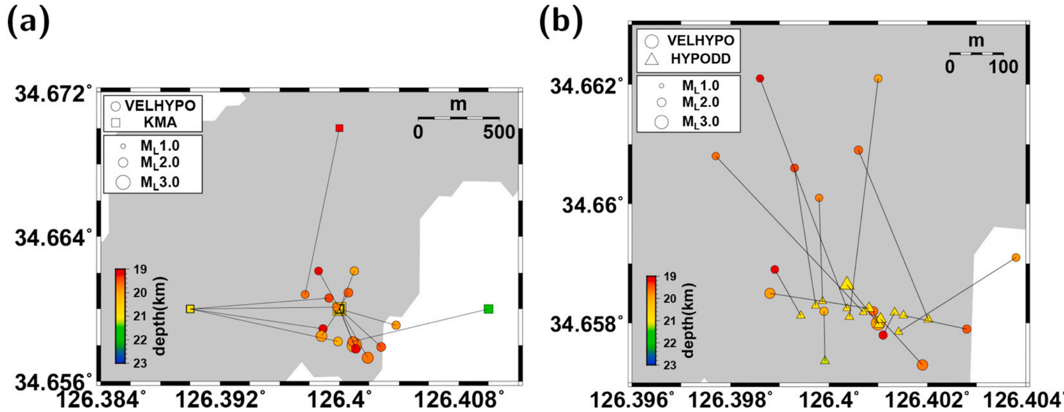

Fig. 5. Hypocenter refinement: (a) hypocenters refined by VELHYPO and the hypocenters reported by KMA, and (b) hypocenters refined by hypoDD for the initial locations based on the results from VELHYPO.

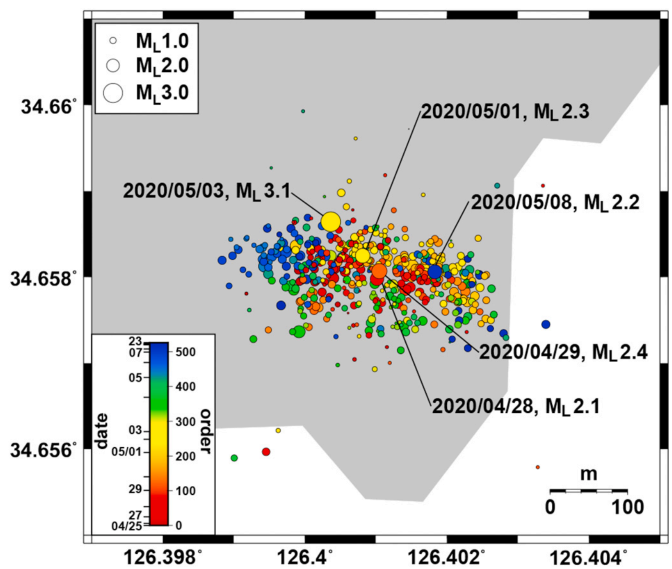

Fig. 6. Map view of the epicenters of the detected earthquakes. Earthquakes with magnitudes $\geq M_L 2.0$ are indicated. The occurrence dates and order are marked.

rapidly through small to micro events.

7. Temporal earthquake distribution

The earthquake swarm started on 26 April 2020. Earthquakes occurred rapidly until 9 May but stopped suddenly since 10 May. Three events with magnitudes of $M_L 0.8$–1.4 occurred in 3 and 14 days. We find two seismicity peaks on 30 April and 3 May 2020 (Fig. 8). On the other hand, the daily emitted energy (seismic moment) is generally constant from April 28 to May 5. We find an instant increase in the emitted seismic energy and earthquakes on 3 May due to aftershocks following the $M_L 3.1$ earthquake. The earthquakes occurred during a limited time period. The temporal distribution presents a one-off appearance of seismic activity. The observation is similar to the earthquake swarms following the 2011 Tohoku-Oki megathrust earthquake (earthquake swarms in regions A, B, and C shown in Fig. 1a).

8. Focal mechanism solutions

We determine the focal mechanism solutions of 9 earthquakes with magnitudes of $M_L 1.8$–3.1 using seismic polarity analysis (Snoke, 2002). The number of stations varies between 26 and 49 depending on the event magnitude. The azimuthal coverage of stations is dense enough to resolve the focal mechanism solutions reasonably well (Fig. 9).

The focal mechanism solutions are similar among the events and suggest left-lateral strike-slip faults (Fig. 9). The strikes are 103.6° ± 3.2°, and the dips are 73.3° ± 11.7°. The strikes from the focal mechanism solutions are consistent with the spatial distribution of events (Fig. 10). Additionally, the focal mechanism solutions are close to those of the earthquake swarm in 2013 (region A in Fig. 1).

The compression (P) axis is oriented 58.5° ± 3.7°, and the tension (T) axis is directed 145.5° ± 3.0°. The inverted stress field is generally consistent with the ambient stress field (with the P axis oriented 73° and T axis directed 163°) (Hong et al., 2015, 2017b; Lee et al., 2017). These observations suggest that the earthquakes occurred in response to the ambient stress field.

The fault type and strike orientations are consistent with those

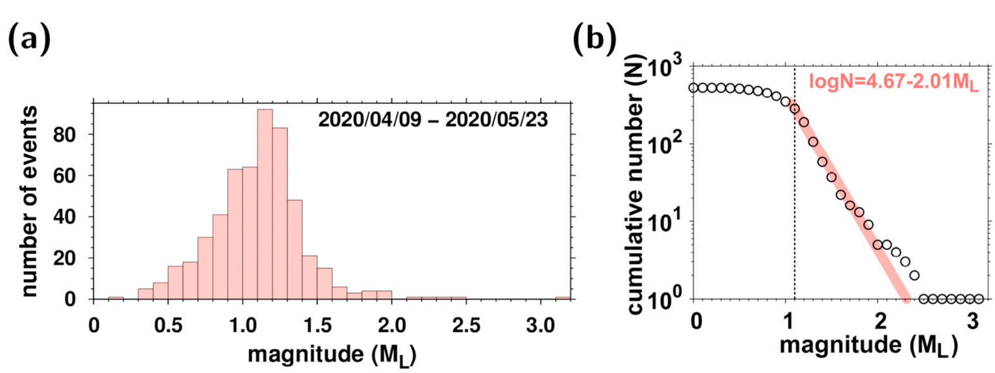

Fig. 7. Magnitude distribution of the earthquake swarm: (a) histogram of earthquake magnitudes (M_L) and (b) Gutenberg-Richter frequency-magnitude relationship. The b value is determined by 2.01 (± 0.05). The minimum magnitude to ensure record completeness is $M_L 1.1$.

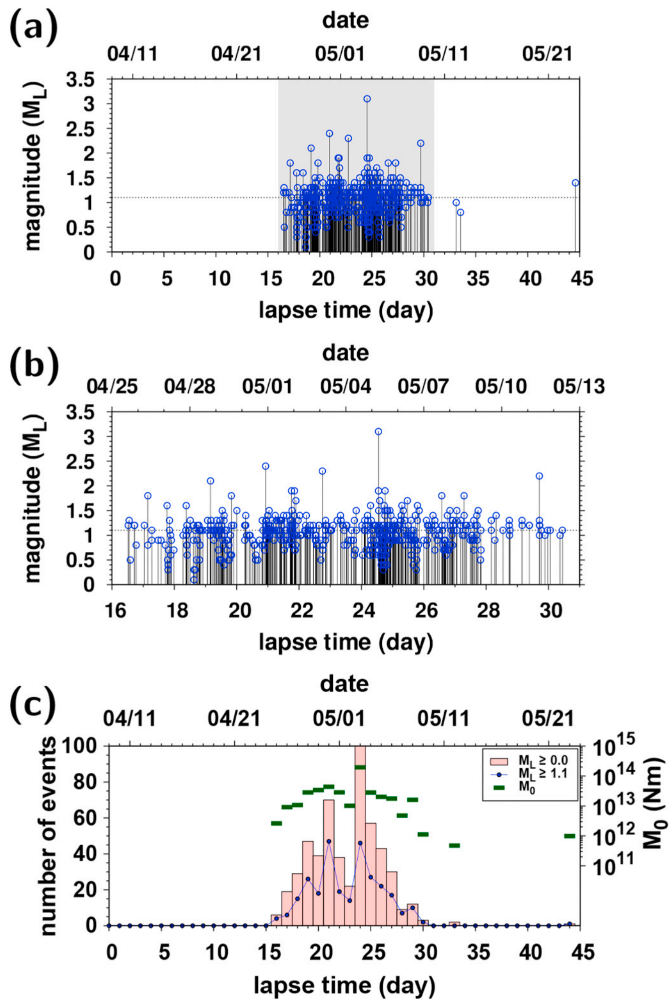

Fig. 8. Temporal distribution of earthquakes: (a) earthquake magnitude distribution with the lapse time, (b) enlarged temporal event distribution, and (c) daily numbers of events and daily emitted energy (given as the seismic moment).

observed in the Korean Peninsula. The observed focal mechanism solutions may preclude the possible influence of deep fluids as an earthquake excitation mechanism. It was reported that fluids may induce normal faulting earthquakes in the deep crust (Gardonio et al., 2018).

9. Spatial earthquake distribution and fault geometry

The earthquakes are spatially clustered. Also, the inverted fault plane solutions (focal mechanism solutions) are nearly same among the events (Fig. 10). The fault plane solutions and spatial distribution of events illuminate an apparent single major fault plane. The events are distributed on a fault plane with dimensions of 500 m by 300 m (Fig. 10). The event distribution suggests that the fault plane is oriented WNW-ESE and dips toward the SW. The lateral distribution of events is consistent with the the strikes of the focal mechanism solutions (Fig. 10).

The events occurred dominantly at depths of 20.9–21.1 km. The occurrence of earthquakes in a narrow depth range may suggest preferential lateral rupture propagation. The M_L3.1 earthquake occurred on the upper western margin of the fault plane. Aftershocks followed the M_L3.1 earthquake around the hypocenter.

The vertical event distribution illuminates a fault plane with a dip angle of 58°, which is lower than the dip angles obtained from the focal mechanism solutions (73.3° ± 11.7°). However, considering the narrow focal depth range of the events, the vertical event distribution is generally consistent with the depth range from the focal mechanism solutions. The high-angle fault plane appears to be effective for left-lateral strike-slip motion.

10. Seismicity evolution

The temporal variation in seismicity reflects the one-off episodic occurrence of earthquakes over time (Fig. 8). The earthquake swarm presents a characteristic spatiotemporal evolution (Fig. 11). In the first phase (phase I) between 25 April and 30 April, the earthquakes occurred in the central area on the fault plane. The earthquakes migrated upward in the second phase (phase II) between May 1 and May 3, occurring around the upper fault margin. Earthquakes moved downward in the third phase (phase III) and occurred mainly around the lower fault margin. Phase III is the period between 3 May and 5 May. The earthquakes migrated laterally in phase IV (between 5 May and 23 May) and occurred on both margins of the fault plane.

The spatiotemporal evolution of seismicity suggests that the earthquake occurrence area expanded with time. The early earthquakes occurred in the central area and expanded radially along the fault plane. The seismicity ceased after phase IV. The seismicity distribution suggests that the fault presented a bilateral rupture. Brittle deformation was effective at a depth of ~21 km, which may have facilitated additional earthquakes depending on the stress level.

11. Faulting mechanism

Deep crustal focal depths and strike-slip motions suggest that the faulting source is not associated with local surface effects. The inverted stress field responsible for the left-lateral strike-slip motion is generally consistent with the ambient stress field. The strike of the seismogenic fault agrees with the general features of earthquakes in the Korean Peninsula.

No active crustal-scale tectonic activity is evident in the source region. Additionally, the crustal temperatures and surface heat flows are lower than most regions in the Korean Peninsula, which suggests no apparent thermoelastic stress effect in the region (Fig. 2). The low temperatures in the source region appear to compose an environment that accommodates deep crustal earthquakes.

The rapid occurrence of earthquakes in the deep crust suggests the rapid emission of stress in a high-pressure environment. It was suggested that lithostatic loading and rapid crustal stress change induced by the 2011 Tohoku-Oki megathrust earthquake may have been responsible for the stress field change (Hong et al., 2015, 2017a).

12. Coulomb stress changes

We estimate the Coulomb stress changes for optimally oriented strike-slip faults (Fig. 12a). We assess the Coulomb stress changes induced by earthquakes with magnitudes of $M_L > 2.0$. The number of earthquakes is 5. The event magnitudes are M_L3.1, 2.4, 2.3, 2.2, and 2.1. The target depth is 21 km. We assume that the local magnitude (M_L) is equivalent to the moment magnitude (M_W). We consider the rupture plane size to be 450 m by 250 m considering the spatial distribution of earthquakes before the M_L3.1 earthquake. The induced stress increased in the directions of WNW-ESE and NNE-SSW from the fault (Fig. 12). The spatial distribution of earthquakes is generally consistent with the induced stress field.

We examine the possible induction of earthquakes along the fault as a result of the emission of stress from the earthquake swarm. We consider a fault geometry with a strike of 104° and a dip angle of 58° (Fig. 12b). We calculate the Coulomb stress changes for the inverted fault geometry. These Coulomb stress changes are similar to those for the optimally oriented strike-slip faults. Stress accumulates strongly, particularly at both horizontal edges of the rupture plane. The induced

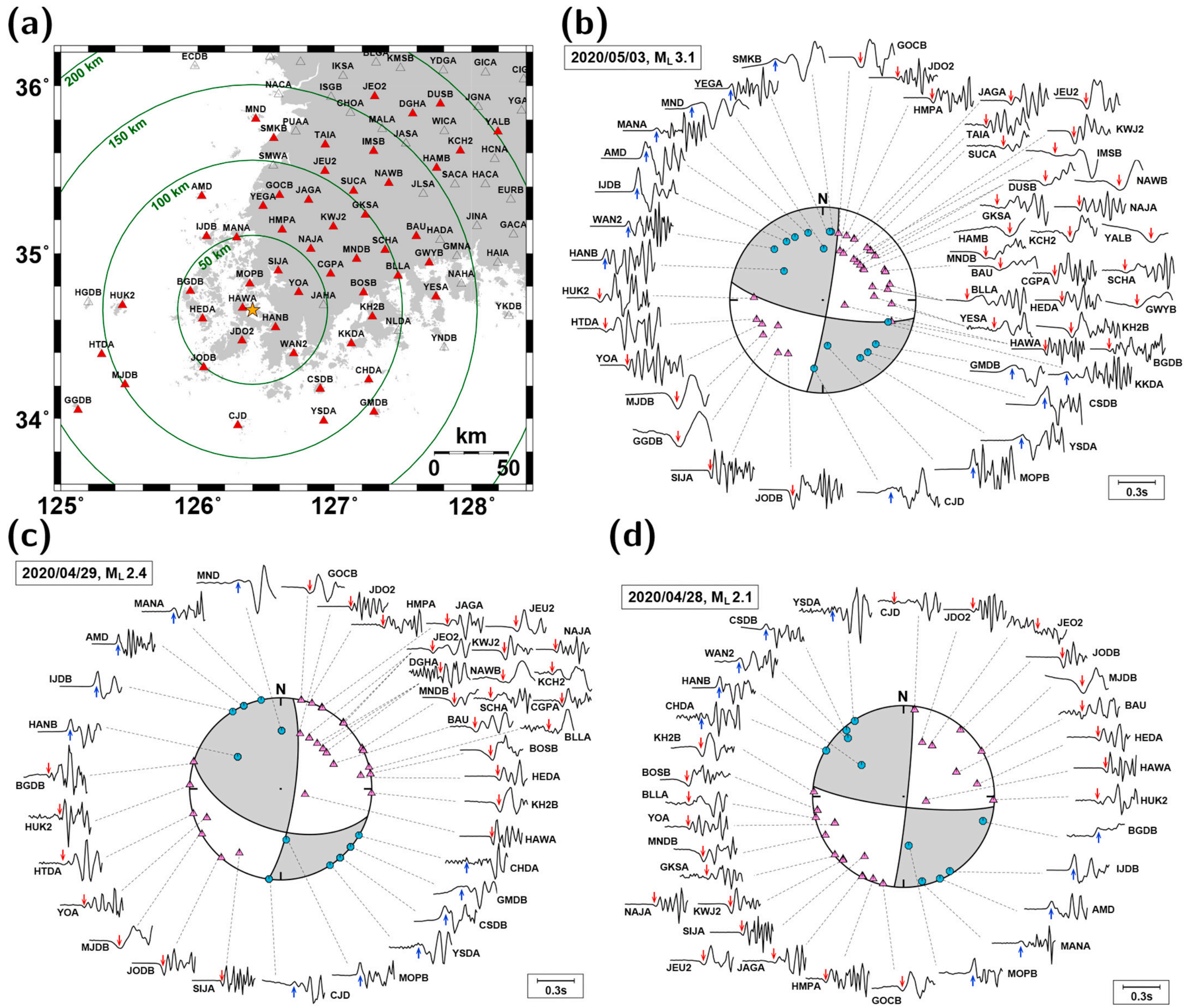

Fig. 9. Examples of the inverted focal mechanism solutions for three earthquakes: (a) map of the seismic stations and earthquake swarm and the inverted fault plane solutions and P waveforms of the (b) 3 May 2020 M_L3.1 earthquake, (c) 29 April 2020 M_L2.4 earthquake, and (d) 28 April 2020 M_L2.1 earthquake.

stress is less than 0.5 kPa at distances > 3 km (Fig. 12c). It is noteworthy that a fractional static stress change may trigger earthquakes in near-critical faults (Stein, 1999). The observed Coulomb stress changes suggest possible triggering of earthquakes near the lateral rupture margins along the fault strike depending on the the fault condition.

13. Discussion and conclusions

We investigated a deep crustal earthquake swarm in the southwestern Korean Peninsula. The deep crustal strike-slip earthquake swarm began on 26 April 2020, and lasted for 15 days. We found 527 earthquakes with magnitudes $\leq M_L$3.1 using matched filter analysis. A few small events followed the earthquake swarm with lapse times of 3 and 14 days. The earthquake swarm was transiently active. The magnitudes of the events were determined using an amplitude scaling factor. The earthquakes were concentrated along a fault plane with dimensions of 500 m by 300 m at a depth of ~21 km.

The seismicity has a Gutenberg-Richter b value of 2.01 (± 0.05), which is 2.2 times larger than the b value (0.92) for the whole Korean Peninsula. The focal mechanism solutions are nearly same among the events. The focal mechanism solutions suggest a left-lateral strike-slip fault with a strike of 103.6° ± 3.2° and a dip of 73.3° ± 11.7°. The orientation of the stress field responsible for the earthquake swarm is consistent with the ambient stress field.

The spatial distribution of events illuminates the fault dimensions and geometry, which are generally consistent with the focal mechanism solutions. The earthquake swarm began in the central area and then migrated outward along the fault plane with time. The spatiotemporal seismicity distribution presents a bilateral rupture motion. The low temperatures in the source region produce an environment that accommodates earthquakes at lower crustal depths.

The Coulomb stress changes increased in the directions of WNW-ESE and NNE-SSW from the fault by the earthquake swarm. A fractional stress change may trigger earthquakes at faults in near critical stress level (Stein, 1999). Earthquakes may occur in the increased stress regions depending on the local stress level.

The deep crustal earthquakes suggest possible reactivation of hidden faults in the lower crust. Low crustal temperature in the southwestern peninsula fosters an environment to have deep crustal earthquakes. The focal mechanism solutions suggest that the

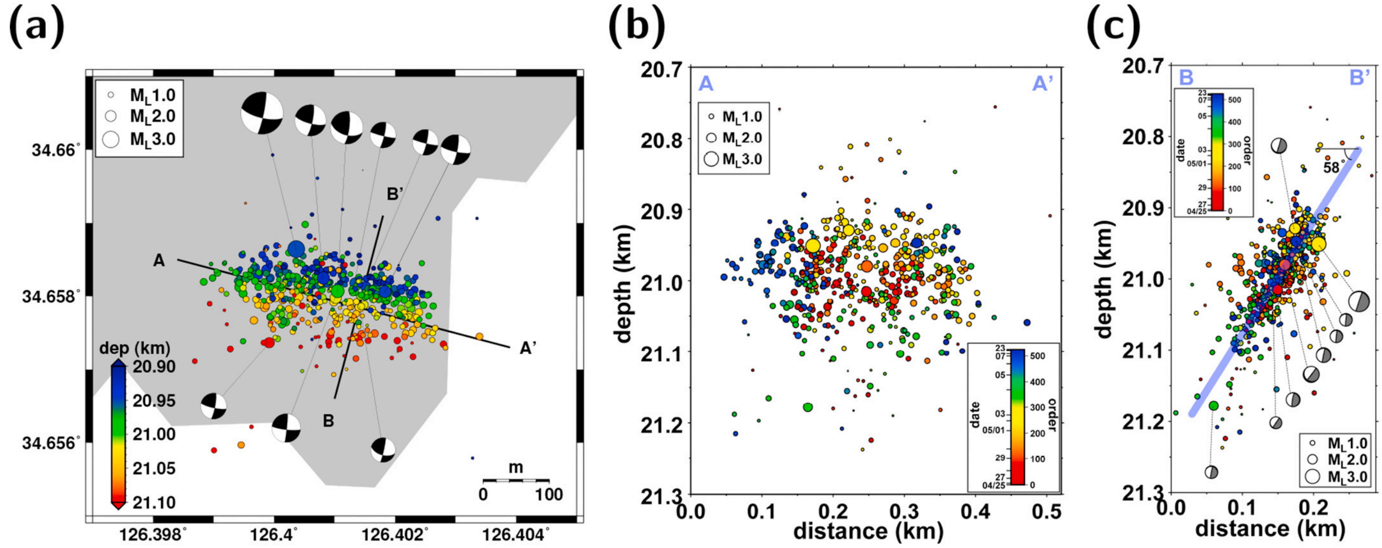

Fig. 10. Spatial distribution of earthquakes: (a) epicenter distribution and (b) vertical event distribution along profiles (b) AA' and (c) BB'. The focal mechanism solutions are presented. The inferred fault dip angle is 58°.

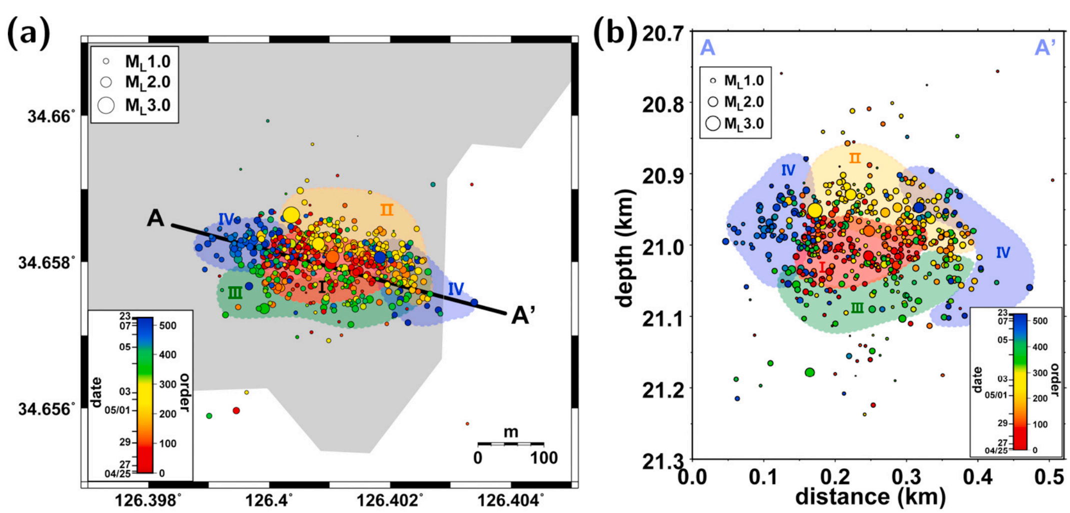

Fig. 11. Spatiotemporal evolution of seismicity: (a) map view of the event distribution with the time period and (b) evolution of seismicity along the fault strike. Four time periods are presented (phases I, II, III, and IV). The seismicity expands outward from the central area on the fault plane.

earthquake swarm might occur as a response to ambient lithostatic stress loading. The unusual deep crustal earthquake surge suggests temporal changes in deep crustal medium properties or stress field. Further, the transiently active earthquake swarm may suggest dynamic interaction between the stress field and deep-crustal fault.

The transiently active earthquake swarm started to occur since the 2011 M_W9.0 Tohoku-Oki megathrust earthquake. The earthquake swarms are distributed in shallow to deep crusts, suggesting possible medium-property change over the crust. It was reported that the 2011 megathrust earthquake lowered the yield strength in the Korean Peninsula (Hong et al., 2015, 2017a, 2018). The transient tension field activated by the 2011 Tohoku-Oki earthquake might cause fluid diffusion in the media, lowering the yield strength in the media (Hong et al., 2015; Yoshida and Hasegawa, 2018; Yoshida et al., 2019).

Intraplate regions have long recurrence intervals of earthquakes. The lithostatic stress is slowly loaded in media for long time. There are media with stress in near critical level. The lowered yield strengths may compose environments to boost continuous and rapid occurrence of earthquakes in media of near critical stress level. The occurrence mechanisms of the earthquake swarms in the Korean Peninsula are similar to those of inland earthquake swarms in Japanese islands since the 2011 Tohoku-Oki megathrust earthquake (Yoshida and Hasegawa, 2018; Yoshida et al., 2019). The occurrence of earthquake swarm in 2020 suggests that the crustal perturbation by the 2011 Tohoku-Oki megathrust earthquake is not fully recovered in the Korean Peninsula, affecting the seismicity persistently.

Declaration of Competing Interest

None

Acknowledgments

We thank Professor Vernon Cormier (editor) and two anonymous reviewers for constructive review comments. The seismic records were collected from Korean Meteorological Administration (KMA) and Korea Institute of Geoscience and Mineral Resources (KIGAM). This work was supported by the Korea Meteorological Administration Research and Development Program under grant KMI2018-02910. Additionally, this research was partly supported by the Basic Science Research Program of National Research Foundation of Korea (NRF-2017R1A6A1A07015374, NRF-2018R1D1A1A09083446).

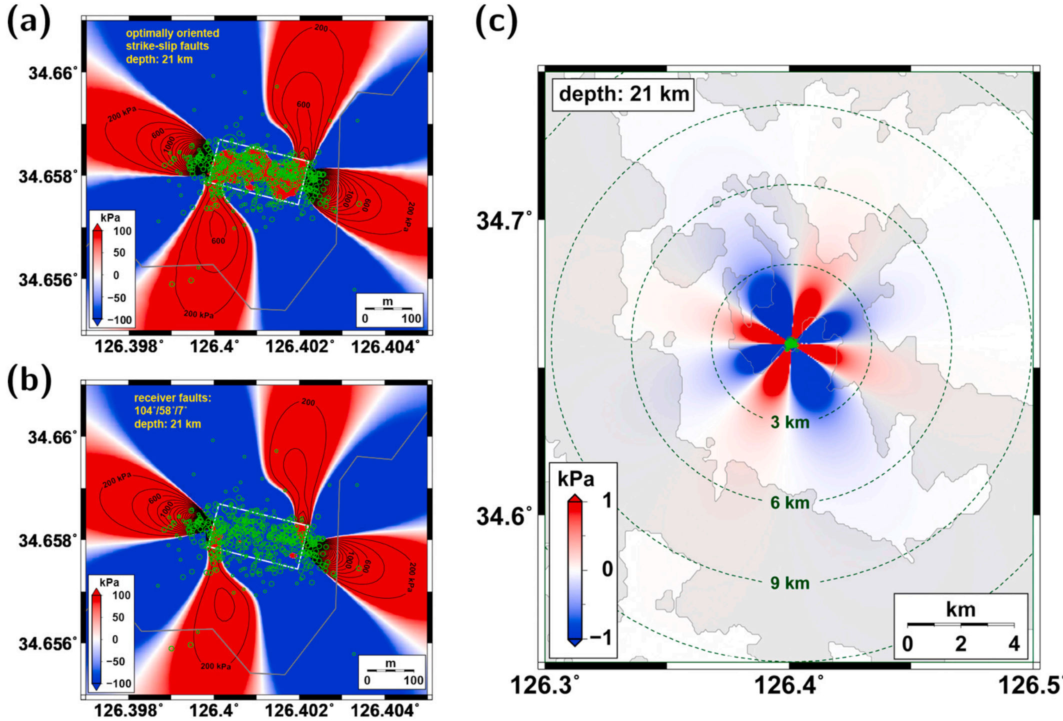

Fig. 12. Induced Coulomb stress changes: Coulomb stress changes induced by earthquakes for the (a) optimally oriented strike-slip faults, (b) illuminated fault geometry, and (c) regional stress field perturbation. The seismicity is marked. The fault plane dimensions are marked by the rectangle.

References

National Emergency Management Agency, 2012. Active faults and seismic hazard map. National Emergency Management Agency, Seoul NEMA-Jayeon-2009-24, 882 p.

Aki, K., 1965. Maximum likelihood estimate of b in the formula log $N = a - bM$ and its confidence limits. Bull. Earthq. Res. Inst. Tokyo University 43, 237–239.

Bender, B.K., 1983. Maximum likelihood estimation of *b* values for magnitude grouped data. Bull. Seismol. Soc. Am. 73 (3), 831–851.

Bonner, J.L., Blackwell, D.D., Herrin, E.T., 2003. Thermal constraints on earthquake depths in California. Bull. Seismol. Soc. Am. 93 (6), 2333–2354.

Brace, W.F., Byerlee, J.D., 1966. Stick-slip as a mechanism for earthquakes. Science 153, 990–992.

Brace, W.F., Byerlee, J.D., 1970. California earthquakes: why only shallow focus? Science 168, 1573–1575.

Brandes, C., Plenefisch, T., Tanner, D.C., Gestermann, N., Steffen, H., 2018. Evaluation of deep crustal earthquakes in northern Germany- Possible tectonic causes. Terra Nova 31, 83–93.

Calais, E., Camelbeeck, T., Stein, S., Liu, M., Craig, T.J., 2016. A new paradigm for large earthquakes in stable continental plate interiors. Geophys. Res. Lett. 43. https://doi.org/10.1002/2016GL070815.

Chen, W., Molnar, P., 1983. Focal depths of intracontinental and intraplate earthquakes and its implications for the thermal and mechanical properties of the lithosphere. J. Geophys. Res. 88, 4183–4214.

Cho, J.-D., Choi, J.-H., Lim, M.-T., Park, I.-H., Ko, I.-S., 1997. A Study on the regional gravity anomaly (Southern Part of Korean Peninsula), KIGAM Research Report KR-96 (c)-5. Korea Institute of Geology and Mining and Material, pp. 27 (in Korean).

Choi, H., Hong, T.-K., He, X., Baag, C.-E., 2012. Seismic evidence for reverse activation of a paleo-rifting system in the East Sea (Sea of Japan). Tectonophysics 572-573, 123–133.

Chough, S.K., Kwon, S.-T., Ree, J.-H., Choi, D.-K., 2000. Tectonic and sedimentary evolution of the Korean Peninsula: a review and new view. Earth-Sci. Rev. 52, 175–235.

Furumura, T., Hong, T.-K., Kennett, B.L.N., 2014. Lg wave propagation in the area around Japan: observations and simulations. Prog. Earth Planet. Sci. 1, 10. https://doi.org/10.1186/2197-4284-1-10.

Gardonio, B., Jolivet, R., Calais, E., Leclere, H., 2018. The April 2017 Mw6.5 Botswana earthquake: an intraplate event triggered by deep fluids. Geophys. Res. Lett. 45, 8886–8896.

Gibbons, S.J., Ringdal, F., 2006. The detection of low magnitude seismic events using array-based waveform correlation. Geophys. J. Int. 165, 149–166.

Hirata, N., Karp, B.Y., Yamaguchi, T., Kanazawa, T., Suyehiro, K., Kasahara, J., Shiobara, H., Shinohara, M., Kinoshita, H., 1992. Oceanic crust in the Japan Basin of the Japan Sea by the 1990 Japan-USSR expedition. Geophys. Res. Lett. 19, 2027–2030.

Hong, T.-K., 2010. *Lg* attenuation in a region with both continental and oceanic environments. Bull. Seismol. Soc. Am. 100, 851–858.

Hong, T.-K., Kang, T.-S., 2009. Pn travel-time tomography of the paleo-continental-collision and rifting zone around Korea and Japan. Bull. Seismol. Soc. Am. 99, 416–421.

Hong, T.-K., Lee, K., 2012. m_b(Pn) scale for the Korean Peninsula and site-dependent *Pn* amplification. Pure Appl. Geophys. 169, 1963–1975.

Hong, T.-K., Baag, C.-E., Choi, H., Sheen, D.-H., 2008. Regional seismic observations of the 9 October 2006 underground nuclear explosion in North Korea and the influence of crustal structure on regional phases. J. Geophys. Res. 113, B03305. https://doi.org/10.1029/2007JB004950.

Hong, T.-K., Lee, J., Houng, S.E., 2015. Long-term evolution of intraplate seismicity in stress shadows after a megathrust. Phys. Earth Planet. Inter. 245, 59–70.

Hong, T.-K., Park, S., Houng, S.E., 2016. Seismotectonic properties and zonation of the far-eastern Eurasian plate around the Korean Peninsula. Pure Appl. Geophys. 173 (4), 1175–1195.

Hong, T.-K., Lee, J., Chi, D., Park, D., 2017a. Seismic velocity changes in the backarc continental crust after the 2011 M_w 9.0 Tohoku-Oki megathrust earthquake. Geophys. Res. Lett. 44, 10997–11003. https://doi.org/10.1002/2017GRL075447.

Hong, T.-K., Lee, J., Kim, W., Hahm, I.-K., Woo, N.C., Park, S., 2017b. The 12 September 2016 M_L 5.8 mid-crustal earthquake in the Korean Peninsula and its seismic implications. Geophys. Res. Lett. 44, 3131–3138. https://doi.org/10.1002/2017GL072899.

Hong, T.-K., Lee, J., Park, S., Kim, W., 2018. Time-advanced occurrence of moderate-size earthquakes in a stable intraplate region after a megathrust earthquake and their seismic properties. Sci. Rep. 8, 13331. https://doi.org/10.1038/s41598-018-31600-5.

Hong, T.-K., Park, S., Lee, J., Kim, W., 2020. Spatiotemporal seismicity evolution and seismic hazard potentials in the western East Sea (Sea of Japan). Pure Appl. Geophys. 177 (8), 3761–3774 (in press).

Houng, S.E., Lee, J., Hong, T.-K., 2016. Dynamic seismic response of a stable intraplate region to a megathrust earthquake. Tectonophysics 689, 67–78.

Jo, E., Hong, T.-K., 2013. Vp/Vs ratios in the upper crust of the southern Korean Peninsula and their correlations with seismic and geophysical properties. J. Asian Earth Sci. 66, 204–214.

Jolivet, L., Tamaki, K., Fournier, M., 1994. Japan Sea, opening history and mechanism: a synthesis. J. Geophys. Res. 99 (22), 237–22,259.

Kennett, B.L.N., Engdahl, E.R., Buland, R., 1995. Constraints on seismic velocities in the Earth from travel times. Geophys. J. Int. 122, 108–124.

Kim, S.-K., Bae, T.-S., 2012. Analysis of crustal deformation on the Korea Peninsula after the 2011 Tohoku earthquake. J. Korean Soc. Surv. Geod. Photogramm. Cartogr. 30, 87–96 (in Korean).

Kim, H.-J., Han, S.-J., Lee, G.H., Huh, S., 1998. Seismic study of the Ulleung Basin crust and its implications for the opening of the East Sea (Japan Sea). Mar. Geophys. Res. 20, 219–237.

Kim, W., Hong, T.-K., Kang, T.S., 2014. Hypocentral parameter inversion for regions with poorly known velocity structures. Tectonophysics 627, 182–192.

Kim, D., Park, K.D., Ha, J., Sohn, D.H., Won, J., 2016a. Geodetic analysis of post-seismic crustal deformations occurring in South Korea due to the Tohoku-Oki earthquake. KSCE J. Civ. Eng. 20, 2885–2892.

Kim, W., Hong, T.-K., Lee, J., Taira, T.A., 2016b. Seismicity and fault geometry of the San Andreas fault around Parkfield, California and their implications. Tectonophysics 677, 34–44.

King, G.C.P., Stein, R.S., Lin, J., 1994. Static stress changes and the triggering of earthquakes. Bull. Seismol. Soc. Am. 84, 935–953.
Kolawole, F., Atekwana, E.A., Malloy, S., Stamps, D.S., Grandin, R., Abdelsalam, M.G., Leseane, K., Shemang, E.M., 2017. Aeromagnetic, gravity, and differential Interferometric synthetic aperture radar analyses reveal the causative fault of the 3 April 2017 Mw 6.5 Moiyabana, Botswana, earthquake. Geophys. Res. Lett. 44, 8837–8846.
Lee, Y., Park, S., Kim, J., Kim, H.C., Koo, M.H., 2010. Geothermal resource assessment in Korea. Renew. Sust. Energ. Rev. 14, 2392–2400.
Lee, J., Hong, T.-K., Chang, C., 2017. Crustal stress field perturbations in the continental margin around the Korean Peninsula and Japanese islands. Tectonophysics 718, 140–149.
Leyton, F., Pérez, A., Campos, J., Rauld, R., Kausel, E., 2009. Anomalous seismicity in the lower crust of the Santiago Basin, Chile. Phys. Earth Planet. Inter. 175, 17–25.
Li, Q., Liu, M., Stein, S., 2009. Spatiotemporal complexity of continental intraplate seismicity: insights from geodynamic modeling and implications for seismic hazard estimation. Bull. Seismol. Soc. Am. 99, 52–60.
McKenzie, D., Jackson, J., Priestley, K., 2005. Thermal structure of oceanic and continental lithosphere. Earth Planet. Sci. Lett. 233, 337–349.
Nalbant, S.S., Hubert, A., King, G.C., 1998. Stress coupling between earthquakes in Northwest Turkey and the North Aegean Sea. J. Geophys. Res. 103, 24469–24486.
Oh, C.W., 2006. A new concept on tectonic correlation between Korea, China and Japan: histories from the late Proterozoic to Cretaceous. Gondwana Res. 9, 47–61.
Park, S., Baek, I., Hong, T.-K., 2020. Six major historical earthquakes in the Seoul metropolitan area during the Joseon dynasty (1392-1910). Bull. Seismol. Soc. Am. https://doi.org/10.1785/0120200004. (in press).
Peng, Z., Zhao, P., 2009. Migration of early aftershocks following the 2004 Parkfield earthquake. Nat. Geosci. 2, 877–881.
Prieto, G., Froment, B., Yu, C., Poli, P., Abercrombie, R., 2017. Earthquake rupture below the brittle-ductile transition in continental lithospheric mantle. Sci. Adv. 3, e1602642.
Schrank, C.E., Fusseis, F., Karrech, A., Regenauer-Lieb, K., 2012. Thermal-elastic stresses and the criticality of the continental crust. Geochem. Geophys. Geosyst. 13, Q09005. https://doi.org/10.1029/2012GC004085.
Shelly, D.R., Beroza, G.C., Ide, S., 2007. Non-volcanic tremor and low-frequency earthquake swarms. Nature 446, 305–307.
Snoke, J.A., 2002. FOCMEC: FOcal MEChanism determinations. In: Lee, W.H.K., Kanamori, H., Jennings, P.C., Kisslinger, C. (Eds.), International Handbook of Earthquake and Engineering Seismology, Part B. Academic Press, San Diego, pp. 1629–1630.
Stein, R.S., 1999. The role of stress transfer in earthquake occurrence. Nature 402, 605–609.
Stein, S., and Mazzotti, S. (2007). Continental Intraplate Earthquakes: Science, Hazard, and Plicy Issues. Special Paper 425, Geological Society of America, Boulder, Colorado.
Toda, S., Stein, R.S., Richards-Dinger, K., Bozkurt, S.B., 2005. Forecasting the evolution of seismicity in southern California: Animations built on earthquake stress transfer. J. Geophys. Res. 110, B05S16. https://doi.org/10.1029/2004JB003415.
Veikkolainen, T., Kukkonen, I.T., Tiira, T., 2017. Heat flow, seismic cut-off depth and thermal modeling of the Fennoscandian Shield. Geophys. J. Int. 211, 1414–1427.
Waldhauser, F., Ellsworth, W.L., 2000. A double-difference earthquake location algorithm: method and application to the northern Hayward fault, California. Bull. Seismol. Soc. Am. 90, 1353–1368.
Watts, A.B., Burov, E.B., 2003. Lithospheric strength and its relationship to the elastic and seismogenic layer thickness. Earth Planet. Sci. Lett. 213, 113–131.
Wiemer, S., Wyss, M., 2000. Minimum magnitude of completeness in earthquake catalogs: examples from Alaska, the Western United States, and Japan. Bull. Seismol. Soc. Am. 90, 859–869.
Wong, I.G., Chapman, D.S., 1990. Deep intraplate earthquakes in the western United States and their relationship to temperatures. Bull. Seismol. Soc. Am. 80 (3), 589–599.
Yoshida, K., Hasegawa, A., 2018. Hypocenter migration and seismicity pattern change in the Yamagata.Fukushima border, NE Japan, caused by fluid movement and pore pressure variation. J. Geophys. Res. 123 (6), 5000–5017.
Yoshida, K., Hasegawa, A., Yoshida, T., Matsuzawa, T., 2019. Heterogeneities in stress and strength in Tohoku and its relationship with earthquake sequences triggered by the 2011 M9 Tohoku-Oki earthquake. Pure Appl. Geophys. 176 (3), 1335–1355.
Zhao, B., Wang, W., Yang, S., Peng, M., Qiao, X., Du, R., Nie, Z., 2012. Far field deformation analysis after the Mw9.0 Tohoku earthquake constrained by cGPS data. J. Seismol. 16, 305–313.